# Sputtering and ripples formation by gas cluster ions on LiNbO$_3$ crystal

© *A.E. Ieshkin* [1], *T.S. Ilina* [2], *D.A. Kiselev* [2], *B.R. Senatulin* [2], *E.A. Skryleva* [2],
 *G. Suchaneck* [3], *Yu.N. Parkhomenko* [2]

[1] Moscow State University,
Moscow, Russia
[2] National University of Science and Technology MISiS,
Moscow, Russia
[3] Solid-State Electronics Laboratory,
TU Dresden, Dresden, Germany

E-mail: ieshkin@physics.msu.ru

The work addresses the creation of surface structures on lithium niobate single crystals. Surface topography of lithium niobate surface sputtered with gas cluster ion beams was investigated. Surface ripples induced on the surface were analyzed using power spectral density functions approach, their evolution with ion fluence and their dependence on the cluster ion energy discussed. Sputter yield value was shown to decrease with surface roughness increase, the reasons of the effect are indicated. Local piezoresponse of the rippled surface was studied.

## 1. Introduction

Accelerated cluster ion beams are widely used for surface modification and material analysis. Over the past two decades, gas cluster ions have attracted attention in this area [1,2]. The argon cluster Ar$_n$ is an ensemble of n argon atoms, where n usually lies in the range from a few tens to several thousands. The atoms are held together by the weak van der Waals interaction. After ionizing such a cluster and accelerating it to an energy of $E_0$ of the order of tens keV, each atom of the cluster has a kinetic energy of only a few eV. When colliding with the surface of a solid body, the cluster is easily destroyed, and almost all of its energy is released in a small region several atomic layers deep. Obviously, the physical processes occurring when the surface is irradiated with gas cluster ions are radically different from the processes occurring when using atomic ions [3–5].

The possibility of accurately selecting the kinetic energy of the cluster atoms and, thus, controlling the characteristics of the interaction of clusters with the surface, determines the use of cluster ion beams in analytical techniques. In the Secondary Ion Mass Specroscopy (SIMS), especially organic samples, cluster ions are used as a profiling or analyzing beam, because, unlike atomic ions, large clusters are able to separate analyte molecules from the surface with virtually no destruction of them [6,7]. In the X-ray photoelectron spectroscopy technique (XPS), cluster ions are used for surface cleaning or for depth profiling [8], although the question of selectivity of sputtering (and, consequently, changes in surface composition) of multicomponent matters remains open [9,10].

In the study [11] the surface of lithium niobate LiNbO$_3$ was studied by the XPS method using cluster ions. Crystals of lithium niobate and tantalate are ferroelectrics and are used in acousto-optical and electro-optical devices [12]. The ability to switch domains using an electron or ion beam was demonstrated, for example, to record information [13]. Lithium niobate is used as a substrate for the growth of high-quality epitaxial films GaN and AlN due to the similar parameters of crystal lattices [14]. There are works devoted to the study of the possibility of using ferroelectrics for the implementation of chemical reactions controlled by polarization [15]. In addition to its own catalytic properties, LiNbO$_3$ can be used to control the activity of the catalytic layer for the implementation of molecular detectors. An extensive overview of the properties and applications of lithium niobate is presented in [16].

Practical applications, as well as the development of an understanding of the fundamental properties of ferroelectrics, require high surface quality and precision methods of its research. In our previous study [11] it was shown that a beam of cluster ions with low specific energy (4 eV/atom) allows for high-resolution depth profiling without violating the Li/Ni ratio. On the other hand, the oblique irradiation with cluster ions led to the development of a wave-like relief (the so-called ripples) on the surface. Such ripples degrade the depth resolution of the analytical technique, but they can be useful, for example, for creating devices for optics, sensors, catalytic surfaces [17]. In this paper the process of sputtering LiNbO$_3$ by gas cluster ions, in particular, the regularities of the formation of ripples on its surface, was investigated.

It is well known that when the surface of a solid body is irradiated with atomic ions, ordered structures can form [18,19]. Their appearance is explained by the development of Bradley−Harper instability [20], which arises due to the dependence of the sputtering yield on the local curvature of the surface: depressions are sputtered faster than protrusions. Various nonlinear terms [21] have been proposed to describe the saturation of the growth of structures and other effects. However, in the case of cluster ions, the protrusions are sputtered faster than the depressions [1]. As a result, with normal irradiation with cluster ions, it is possible to achieve smoothing of the surface to subnanometer roughness values. Another reason for the smoothing effect is stimulation of the lateral movement of atoms along the surface when the cluster collides with matter. Precision flattening of the surface with cluster ions may be particularly of interest in the case of lithium niobate [22], taking into account the numerous work on the manufacture of nanostructures on its surface using a co-focused ion beam (FIB) [23] or reactive etching [24], which usually leads to a high surface roughness.

We emphasize that the effect of the formation of ripples by an oblique beam of cluster ions to date does not have a complete theoretical explanation. Only the work [25], in which the asymmetric lateral motion of surface atoms was considered as the cause of their occurrence, can be noted. The occurrence of ripples on metals and semiconductors (gold, copper, silicon) has been experimentally investigated in [26–28], and it has been shown that ripples perpendicular to the plane of incidence of the beam occur in a certain range of angles of incidence (approximately from 30 to 70° from the normal to the surface). In general, their amplitude and wavelength are on the order of tens to hundreds of nanometers and increase with increasing irradiation fluence. The formation of ripples can be controlled by setting the target temperature and thus changing the ratio between smoothing due to isotropic diffusion and the development of roughness due to cluster irradiation [29,30].

The occurrence of ripples on dielectrics has been studied to a much lesser extent. Recently, studies using a single crystal of potassium titanyl phosphate ($KTiOPO_4$, KTP) [31,32] have shown that ripples occur in a low-energy irradiation mode (12.5 eV/atom) and do not occur at an energy of 110 eV/atom. The work of Yamada et al. [33] demonstrated the growth of ripples arising on $SiO_2$ film on silicon, with an increase in fluence. The sputtering yield also depended on the fluence, that is, it changed as the relief developed. This effect is widely discussed for sputtering with atomic ions [34,35], but we are not aware of other works describing it for sputtering with cluster ions. Moreover, the sputtering yield $Y$ (the average number of atoms knocked out by the incident ion) and its dependences on the energy of the cluster are known only for a limited set of matters, although such data are extremely useful for etching with cluster ions. Empirical dependencies describing the dependence of $Y$ on the specific energy $E/n$ (kinetic energy per cluster atom) for this set of materials

at a fixed angle of incidence are proposed in [36,37]. At the same time, data on the dependence of $Y$ on the angle of incidence $\theta$ are quite contradictory. The first measurements of such a relationship for metals ($Cu, Au$) showed a monotonic decrease $Y \propto \cos(\theta)$ [38]. Later, numerical simulations showed that the dependence $Y(\theta)$ is monotonous in the case of sputtering of the original ideal Ag crystal, but acquires a weakly expressed maximum at $\theta \sim 30°$ after modification of its surface with a certain dose of irradiation [39]. The dependence for $SiO_2$ resembled a similar dependence for the case of atomic ions and had a maximum at approximately 60−70 degrees [33].

To describe the surface topography, the values of average ($R_a$) or root-mean-square ($R_{rms}$, $\sigma$ or $RMS$) roughness are usually used. However, often a single statistical quantity can not provide enough information about the structure of the surface, its periodicity, etc. So, surfaces with the same values $R_{rms}$ can have a different nature of the relief. The power spectral density function (PSD) carries more information and describes two aspects of roughness: the range of heights relative to the midplane and the lateral dimensions of the corresponding irregularities [40,41]. In this paper, an analysis of the evolution of the relief formed on the surface of $LiNbO_3$ by a beam of cluster ions was carried out using the PSD formalism, described in more detail in section 3. The sputtering yield $Y$ of lithium niobate by cluster argon ions have been determined, and the effect of surface topography on the value of $Y$ has been studied.

## 2. Material and methods

For the experiments, commercial polished plates $LiNbO_3$ congruent composition with a thickness of 0.5 mm (Elan LLC, St. Petersburg) were used. The plates were oriented in the polar direction $z$, the experiments used a negative surface Z- (note that in the previous study [11] the dependence of the sputtering yield and surface relief on the polarity of Z-cut of plates was not observed). The samples were washed in an ultrasonic bath for 10 minutes sequentially in isopropyl alcohol and deionized water.

Sputtering experiments were carried out at the PHI 5000 VersaProbeII (ULVAC-PHI) unit, equipped with a source of argon cluster ions with energies up to 20 keV. Two geometries of the experiment were implemented: at the angle of incidence of the beam on the sample $\theta = 0°$ (normal incidence) and $\theta = 55°$ (oblique incidence). The average cluster size $n$ was 2500 atoms.

To study the topography of samples irradiated with various fluences of cluster ions, an accelerating voltage of 20 kV was used. In addition, a voltage of 10 kV was used to determine the effect of ion energy. The cluster ion beam was scanned within a rectangular region on the surface of the sample. The ion current measured from the metal sample holder was 88 nA at an accelerating voltage of 20 kV and 29 nA at a voltage of 10 kV. The pressure in the sample chamber was no more than $3 \cdot 10^{-8}$ Pa

before the experiment and about $10^{-5}$ Pa during irradiation. During each sputtering experiments charging of the surface was compensated by low-energy fluxes of electrons and ions.

Etching crater depths were measured with an Alpha-Step IQ stylus profilometer. The measured width of the crater at half-height (FWHM) was used to determine the fluence of ion irradiation.

The topography of the surface was determined by atomic force microscopy (AFM) using the MFP-3D Stand Alone system (Asylum Research, USA) in contact mode. NSG30/Pt (Tipsnano, Estonia) cantilevers with a resonance frequency of 240 kHz and a hardness of $k = 20$ N/m were used. Scan sizes with a resolution of $512 \times 512$ dots were $5 \times 5\,\mu$m, $10 \times 10\,\mu$m and $20 \times 20\,\mu$m, scan speed was 0.8 Hz. The direction of the scan coincided with the direction of the cluster beam incidence. The images were analyzed using the Gwyddion 2.58 package (http://www.gwyddion.net) [42]. Scans data with different sizes were used to calculate the combined PSD function. This approach made it possible to consider the range of spatial wavelengths from 0.31 to $80\,\mu$m$^{-1}$.

In addition, simultaneously with the recording of the topographic signal, a piezoresponse signal was recorded. To do this, a voltage of 3 V was applied to the probe.

The topography of the surface of the samples was also observed in the Zeiss Ultra55 scanning electron microscope (SEM) in the mode of collecting secondary electrons. The image recording at an electron energy of 5 keV was carried out quickly enough to prevent distortions caused by charging.

## 3. Calculation technique

The image of the surface topography in the AFM makes it possible to directly calculate the value $\sigma^2$ as the average square of the height deviations measured in $N$ points of the surface from the average height

$$\sigma = \sqrt{\frac{1}{N}\sum_{n=1}^{N}(h_n - \langle h \rangle)^2}. \qquad (1)$$

For a more complete description, you can use the PSD function. It is the square of the Fourier transform of the surface profile. Thus, it contains information on both the height and lateral dimensions of surface structures. In addition, the PSD function makes it possible to identify spatial frequencies corresponding to periodic features of topography, such as ripples.

Several types of PSD functions are used in the literature, defined in different ways. The two-dimensional function $PSD_{2D}(k_x, k_y)$ can be written as the Fourier transform from an autocorrelation function or as the squared module of Fourier transform of the $h(x, y)$ function describing the topography of the surface. It gives more complete information about the surface. For isotropic surfaces,

you can introduce a radial PSD function $PSD_{2D}(|\vec{r}|)$. In our case of a strongly anisotropic surface, the one-dimensional PSD function $PSD_{1D}(k_x)$, which is an integral of $PSD_{2D}(k_x, k_y)$ by $k_y$ (with a multiplier dependent on the normalization used) was used. According to definitions, functions $PSD_{2D}$ have dimension m$^4$, while dimension of $PSD_{1D}$ — m$^3$.

Mathematically, the „areas" under the PSD graphs of each type coincide (as they coincide for the functions $PSD_{1D}(k_x)$ and $PSD_{1D}(k_y)$) and are equal to the square of $R_{\text{rms}}$ (again, taking into account the multiplier dependent on the normalization). In practice, these values may vary due to effects related to the bandwidth of spatial frequencies, especially in the case of anisotropic surfaces.

So, all the PSD functions in further discussion are $PSD_{1D}$. To determine the experimental combined PSD function of each sample, the geometric mean of the individual PSD function defined for partially overlapping scans was calculated at $5 \times 5\,\mu$m, $10 \times 10\,\mu$m and $20 \times 20\,\mu$m [43]:

$$PSD_{combined} = \left[\prod_{J=1}^{3} PSD_i\right]^{1/3}. \qquad (2)$$

For simplicity, the formula of the geometric mean was used without taking into account the weights, since the PSD function of the various scans in the region of frequency overlap did not differ much.

The experimental combined PSD function were approximated by the sum of two analytical models. *K*-correlation model (or *ABC* model) describes a surface with random roughness. The PSD function given by the *ABC* model is expressed as [44]:

$$PSD_{ABC} = \frac{A/2\pi}{\left(1 + (B/2\pi)^2 k^2\right)^{C/2}}, \qquad (3)$$

where $A$, $B$ and $C$ — model parameters, $k$ — the spatial wave number. Equation (3) describes a monotonically decreasing with increasing frequency of the PSD (usually depicted on a double logarithmic scale). The $A$ parameter describes the low-frequency limit of the spectrum. The physical meaning of the gentle part of this curve is that with such measurements in straight space there are no significant deviations in height. The $B$ parameter defines the correlation length beyond which height fluctuations are not correlated, and the $C$ parameter determines the slope of PSD function.

Given the normalization used in the Gwyddion package, the root mean square roughness $\sigma_{ABC}$ and the correlation length $\tau_{ABC}$ within this model can be calculated as [43,44]:

$$\sigma_{ABC}^2 = \frac{4\pi A'}{B^2(C-1)}, \quad \tau_{ABC}^2 = \frac{2(C-1)^2 B^2}{C}, \qquad (4)$$

where $A'$ — parameter of the two-dimensional PSD function $PSD_{2D}(|\vec{r}|)$ [44]:

$$A' = \frac{AB}{2\sqrt{\pi}} \frac{\Gamma\left(\frac{C+1}{2}\right)}{\Gamma\left(\frac{C}{2}\right)}, \qquad (5)$$

and $\Gamma(\xi)$ — gamma function. It should be noted that such a definition of $\sigma_{ABC}$ applies only to isotropic surfaces (it is obvious that otherwise the two-dimensional PSD function cannot be reconstructed by one-dimensional). Therefore, we assume that the random roughness described by the *ABC* model is quite isotropic.

Local maxima on the PSD function graph corresponding to structures such as ripples are well described by the Gaussian function with a maximum shifted to a non-zero spatial wavenumber $k_{sh}$ [43,45]:

$$PSD_{sh} = \frac{\sigma_{sh}^2 \tau_{sh}}{4\sqrt{\pi}} \exp\left[-\frac{\tau_{sh}^2(k - k_{sh})^2}{4}\right]. \qquad (6)$$

In this formula, $\sigma_{sh}$ and $\tau_{sh}$ — the root mean square roughness and correlation length, respectively, associated with part of the relief described by the Gaussian model. The model corresponds to an autocorrelation function in the form of a product of the Gaussian function multiplied by a harmonic wave. The period of the latter corresponds to the period of surface structures and is determined by $k_{sh}$.

The use of the sum of the $k$-correlation function and Gaussian functions made it possible to achieve a good correspondence with the experimental combined PSD functions:

$$PSD_{sum} = PSD_{ABC} + \sum_{j=1}^{n}(PSD_{sh})_i, \qquad (7)$$

where $n$ — the local maximum number.

The parameters $A$, $B$, $C$, $k_{sh}$, $\sigma_{sh}$, $\tau_{sh}$ were adjusted using EXCEL. The spatial wavelength $\lambda_{sh}$ was defined as $2\pi/k_{sh}$.

# 4. Results and discussion

## 4.1. Surface topography

First of all, consider the evolution of surface topography with the oblique incidence of cluster ions and their fixed energy. SEM images of the lithium niobate surface after sputtering with cluster ions with an energy of $20\,\text{keV}$ at different fluences are shown in Fig. 1. Although such images do not provide quantitative information about the topography, they are very useful for the qualitative observation of the relief form. The smallest fluence used $(0.93 \cdot 10^{16}\,\text{ion/cm}^2)$ resulted in ordered ripples with an average wavelength of about $100-150\,\text{nm}$. Their wave vector lies in the plane of the incidence of the ion beam. Ripples uniformly cover the entire surface. You can see a few scratches left after polishing the surface, and these scratches do not have a noticeable effect on the shape of the ripples.

With an increase in fluence (Fig. 1, $b, c$), a second mode of ripples with a longer wavelength arises. Interestingly, unlike the first mode, such ripples are distributed on the surface inhomogeneously. Their appearance can not be associated with scratches or any other originally existing embryos, apparently, they developed as a result of local

instability. At the largest fluences (Fig. 1, $d, e$), the ripples again become homogeneous, their wavelength is about $0.5-1.5\,\mu\text{m}$. Between the crests of the waves in Fig. 1, $d$ a thin structure is visible in the form of drift lines [11,17,46], while the side of the waves facing the ion beam remains fairly smooth. In Fig. 1, $e$ the crest of the upper wave is broken, which indicates that it hung over the surface. The thin structure has the appearance of drift lines only at the end of the posterior slopes of the waves.

Figure 2 shows atomic force images of the same samples and surface profiles obtained from AFM data. The height span of ripples at the lowest fluence is $4-8\,\text{nm}$. With an increase in fluence, the height of ripples slightly increased, you can see the emergence of a second mode of ripples with large wavelengths and a height of about $20-60\,\text{nm}$. At maximum fluence, the height span is $250-350\,\text{nm}$. The shape of the ripples is asymmetrical. The side facing the ion beam becomes almost perpendicular to its direction, and the opposite side approaches the direction of the beam incidence, that is, to a state where it is obscured by the crest of the wave.

The above description can be quite subjective, while statistical analysis makes it possible to determine the quantitative characteristics of the topography. Fig. 3 shows the experimental combined PSD functions of the irradiated samples and the reference surface.

All experimental curves show features of the model *ABC* (3). In addition, local maxima indicate the presence of periodic structures, that is, ripples; they correspond to Gaussian functions (6). An increase in fluence leads to an increase in the amplitude of the PSD function and a shift in local maxima to the region of large wavelengths. The PSD function of the initial surface is several orders of magnitude smaller than after irradiation. Therefore, the initial roughness of the polished surface does not in itself contribute to the spectral power density functions, the analysis of which is given below.

Summation of the $k$-correlation model and Gaussian functions for approximating experimental PSD functions, Fig. 4, made it possible to obtain a good quality of approximation, with the exception of the low-frequency region for samples with small fluences. This frequency range from 0.3 to $3\,\mu\text{m}^{-1}$ corresponds to wavelengths from 2.1 to $21\,\mu\text{m}$ and contains the first 10 points that are least reliable. The obtained approximation parameters are given in Table 1. The values of $\sigma_{tot}$ given in table are the RMS roughnesses calculated from the area under the corresponding combined PSD function. In general, these values are slightly higher than the values calculated from the approximation parameters as

$$\left(\sigma_{ABC}^2 + \sum_i(\sigma_{sh})_i^2\right)^{1/2}, \qquad (8)$$

in particular, because the sum of $k$-correlation model and Gaussian functions underestimates the PSD function at the first few points, as shown in Fig. 4, $a$. The values of $\sigma_{tot}$
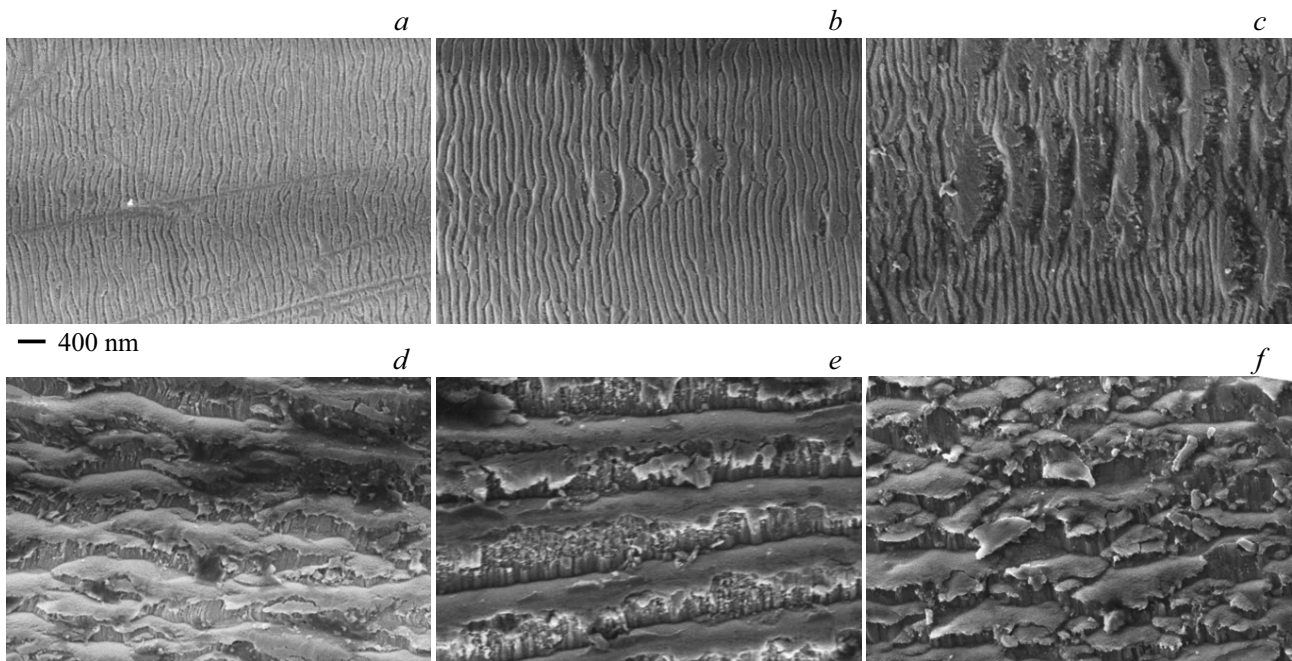
**Figure 1.** SEM images of the surface of lithium niobate after sputtering with cluster ions at oblique incidence ($\theta = 55°$) with an energy of 20 keV and fluences of $0.93 \cdot 10^{16}$ ion/cm$^2$ ($a$), $4.6 \cdot 10^{16}$ ion/cm$^2$ ($b$), $9.3 \cdot 10^{16}$ ion/cm$^2$ ($c$), $19 \cdot 10^{16}$ ion/cm$^2$ ($d$), $56 \cdot 10^{16}$ ion/cm$^2$ ($e$) and with an energy of 10 keV and fluence of $33 \cdot 10^{16}$ ion/cm$^2$ ($f$). The direction of ion incidence — on the left for images ($a-c$) and on top for images ($d-e$).
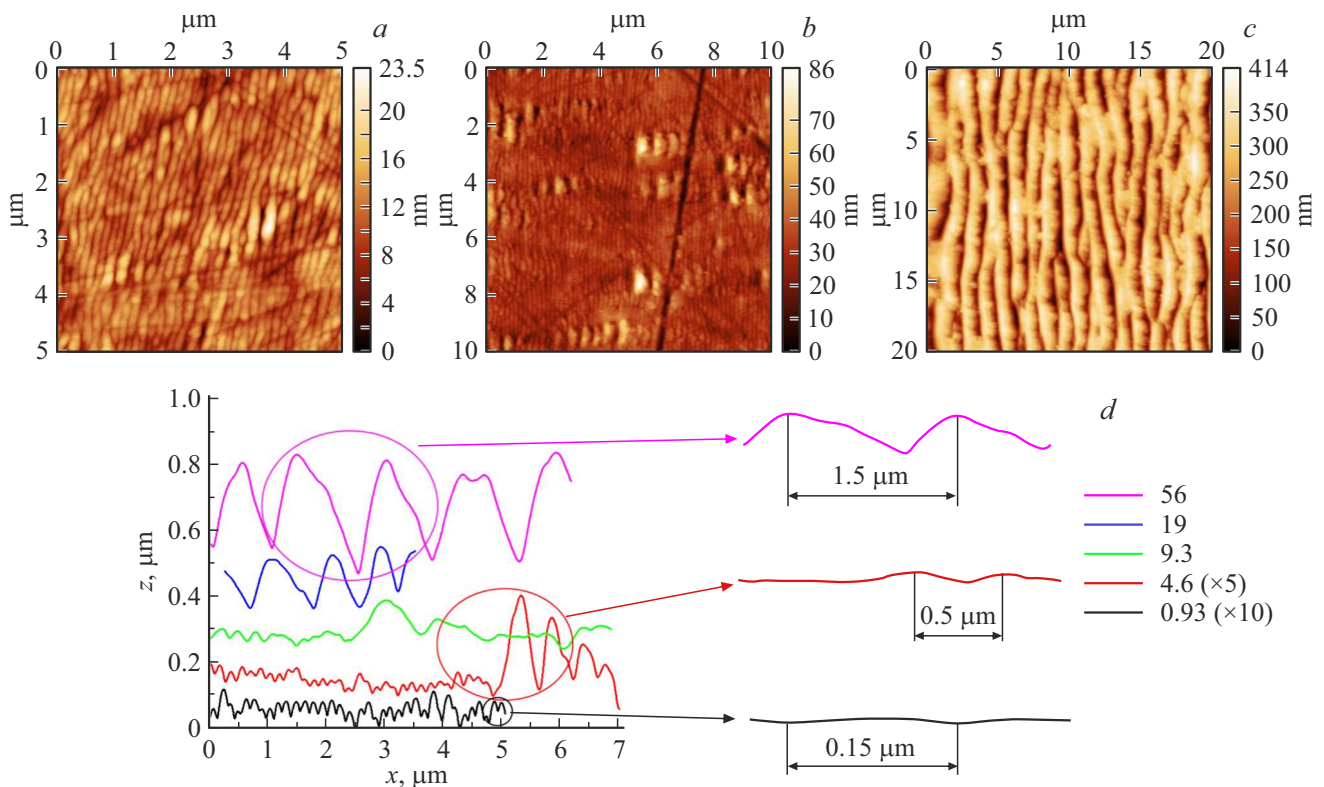


**Figure 2.** AFM images of areas irradiated with fluences $0.93 \cdot 10^{16}$ ion/cm$^2$ ($a$), $4.6 \cdot 10^{16}$ ion/cm$^2$ ($b$), $56 \cdot 10^{16}$ ion/cm$^2$ ($c$). Surface profiles ($d$), fluences are given in units $10^{16}$ ion/cm$^2$. Real forms of profiles are shown. The direction of ion incidence — from the left.

**Table 1.** Parameters of approximation of the PSD function. $\sigma$ — RMS roughness, $\tau$ — correlation length, $\lambda$ — dominant ripple wavelength, $h$ — ripple height span estimated directly from AFM profiles.

| Fluence, $10^{16}$ ions/cm$^2$ | $\sigma_{tot}$, nm | $\sigma_{ABC}$, nm | $\tau_{ABC}$, nm | Characteristics of ripples, nm | | |
|---|---|---|---|---|---|---|
| | | | | $\lambda_{sh}$ | $\sigma_{sh}$ | $h$ |
| 0 | 0.43 | 0.4 | 245 | | | |
| 0.93 | 2.5 | 1.8 | 126 | 151 | 0.50 | 4−8 |
| | | | | 286 | 0.85 | |
| 4.6 | 7.0 | 4.7 | 151 | 165 | 1.1 | 4−10 |
| | | | | 650 | 3.2 | 20−60 |
| 9.3 | 20 | 12 | 201 | 220 | 1.4 | 20−40 |
| | | | | 900 | 9.2 | 50−130 |
| 19 | 55 | 39 | 327 | 816 | 14 | 140−180 |
| | | | | 1210 | 28 | |
| 56 | 69 | 39 | 282 | 1370 | 57 | 250−350 |
| 10 keV, $33 \cdot 10^{16}$ ions/cm$^2$ | 18 | 19 | 276 | 546 | 4.2 | 25−60 |
| | | | | 873 | 7.8 | |
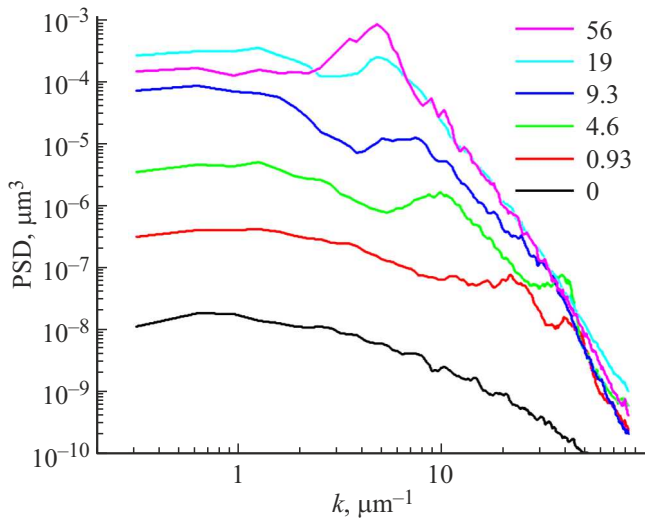


**Figure 3.** Experimental combined PSD functions of lithium niobate samples, irradiated with clusters $Ar_{2500}^+$ with an energy of 20 keV at oblique incidence (fluences in units of $10^{16}$ ion/cm$^2$) and the original sample (fluence 0).

with a wavelength of more than 500 nm, and then to large ripples with $\sigma_{sh} \sim 60$ nm and a wavelength of more than 1.2 $\mu$m. The values of $\lambda_{sh}$, shown in Table 1, coincide with the previous qualitative description. As for the values of $\sigma_{sh}$, recall that for a harmonic wave, the height span is 2.8 times higher than the root mean square roughness. The values $h$ given in Table 1 are more than 2 times higher than the corresponding $\sigma_{sh}$, since (i) the shape of ripples is generally far from harmonic (as can be seen from Fig. 2) and (ii) ripples do not always cover the surface completely (as a mode with $\lambda_{sh} = 650$ nm with fluence $4.6 \cdot 10^{16}$ ion/cm$^2$, Fig. 2, $b$). Thus, $\sigma_{sh}$ can be used to describe the statistical characteristics of ripples, but not their actual heights. Along with ripples, the roughness associated with the $k$-correlation model also increases.

Continuing the discussion of the results obtained, we emphasize that neither AFM nor SEM alone can give an exhaustive picture of topography. Thus, the SEM images show that with significant fluences, the front part of the wave is quite smooth (although it shows a structure formed, apparently, as a result of overlapping craters from individual clusters). On the back slope, drift lines are visible along the direction of movement of the clusters, formed as a result of the reprecipitation and redistribution of target atoms.

Statistical analysis of AFM images provides quantitative information about the heights of the ripples (although their shape at a high aspect ratio can be distorted by the shape of the probe). The anterior slope of the waves at high fluences is almost perpendicular to the surface. Geometric calculations show that at an angle of incidence $\theta = 55°$, a
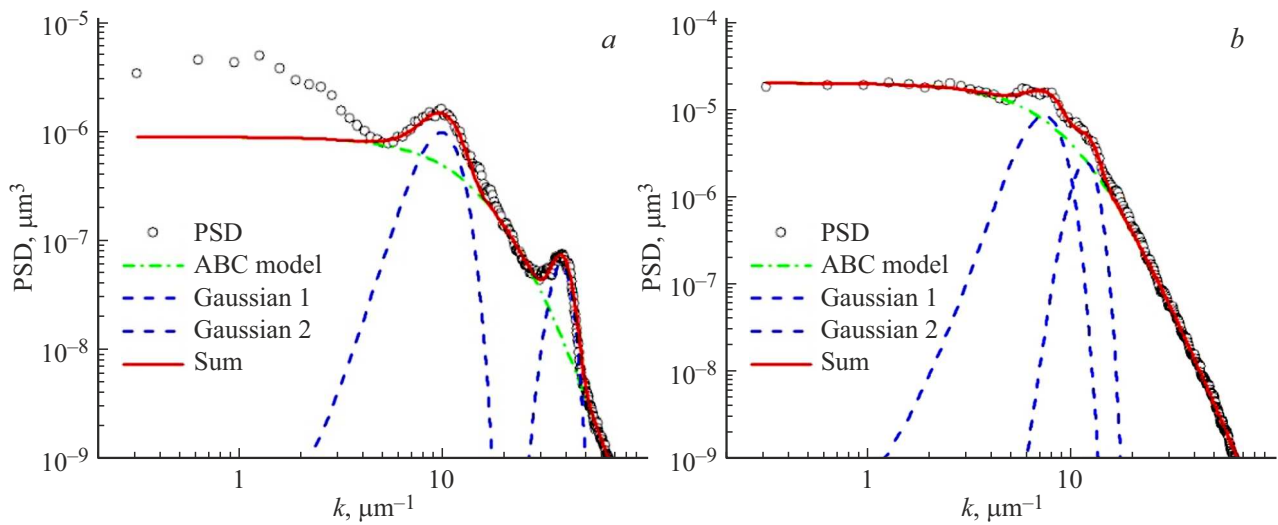
also correspond well to the root mean square roughness calculated directly from the AFM data using (1), which indicates the correctness of our assumptions about $PSD_{1D}$.

As can be seen from Table 1 and Fig. 5, $a$, the dominant wavelength of ripples ($\lambda_{sh}$) and the associated roughness ($\sigma_{sh}$) increase with increasing fluence. There is a transition from small ripples with $\sigma_{sh} \sim 0.5-0.85$ nm and a wavelength of $150-300$ nm to combined structures
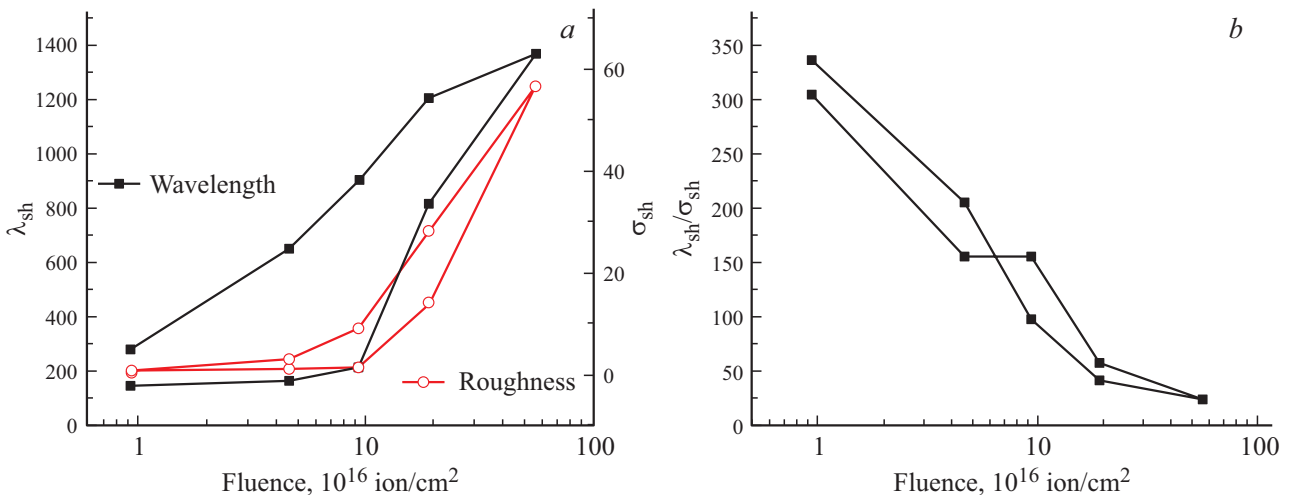
**Figure 4.** Approximation of the experimental combined PSD function with the sum of $k$-correlation model and Gaussian functions for samples irradiated with fluences $4.6 \cdot 10^{16}$ ion/cm$^2$ at 20 keV ($a$) and $33 \cdot 10^{16}$ ion/cm$^2$ at 10 keV ($b$).



**Figure 5.** The dependence of ripple parameters on fluence.

protrusion with a height of $h$ obscures the beginning of the next protrusion if the distance between them $\lambda$ is $2.13h$ (Fig. 6, $c$). The measured ratios of $\lambda_{sh}/h$ decrease with a fluence increase from 25 to $4-5$. The latter values are still larger than 2.13, but we can expect a further decrease in $\lambda_{sh}/h$ up to a stationary value. Of course, this does not mean that in a stationary state the growth of the height of ripples will stop. The monotone descending of $\lambda_{sh}/\sigma_{sh}$ is also shown in Fig. 5, $b$.

It is known that the angular distributions of the sputtered matter by cluster ions are lateral in nature, that is, most of the substance is emitted at high angles from the local normal to the surface. Angular distributions become strongly asymmetric with the oblique incidence of clusters [47]. Thus, the evolution of ripples can be described as shown in Fig. 6. With large $\lambda/h$ (i.e., small fluences), the matter sputtered from the posterior slopes of the waves is

reprecipitated on the front slopes in such a way that the depressions are sputtered faster (cf. [25]). The accumulation of this matter leads to the growth of protrusions, at some point their ridges begin to hang over the back slope. Finally, when the ratio of $\lambda/h$ is close to the shading condition, the overall flow direction of the reprecipitated matter changes to the opposite. This explains the structure between the ripples in Fig. 1, $e$: drift lines appear, directed along the posterior slope of the wave to its crest and interacting with the lines originally directed from the crest downwards.

Let us consider further how the formation of ripples is affected by the energy of clusters. From Fig. 1, $f$ it can be seen that with less energy, the shape of the ripples retains the same features. Quantitative analysis (Fig. 4, $b$, Fig. 5, $b$ and Table 1) makes it possible to obtain roughness parameters. In general, ripples have a fairly large length and low height. However, it makes sense to compare

**Table 2.** Sputtering yield of lithium niobate by cluster ions $Ar_{2500}^+$

| Parameters of sputtering | Fluence, $10^{16}$ ion/cm$^2$ | Depth of craters, nm | $Y$, at/ion | $\sigma_{tot}$, nm |
|---|---|---|---|---|
| Source surface | 0 | – | $34 \pm 5$ | 0.43, scratches |
| 10 keV, 0° | 59 | 45 | $0.72 \pm 0.1$ | < 0.1, without scratches |
| 10 keV, 55° | 33 | −20 (measured) 40 (evaluation) | – | 18 |
| 20 keV, 0° | 97 | 2280 | $22 \pm 2$ | 0.1, scratches |
| 20 keV, 55° | 0.93 | 34 | $34 \pm 5$ | 2.5 |
|  | 4.6 | 162 | $30 \pm 4$ | 7.0 |
|  | 9.3 | 300 | $28 \pm 2$ | 20 |
|  | 19 | 585 | $25 \pm 2$ | 55 |
|  | 56 | 1492 | $23 \pm 2$ | 69 |
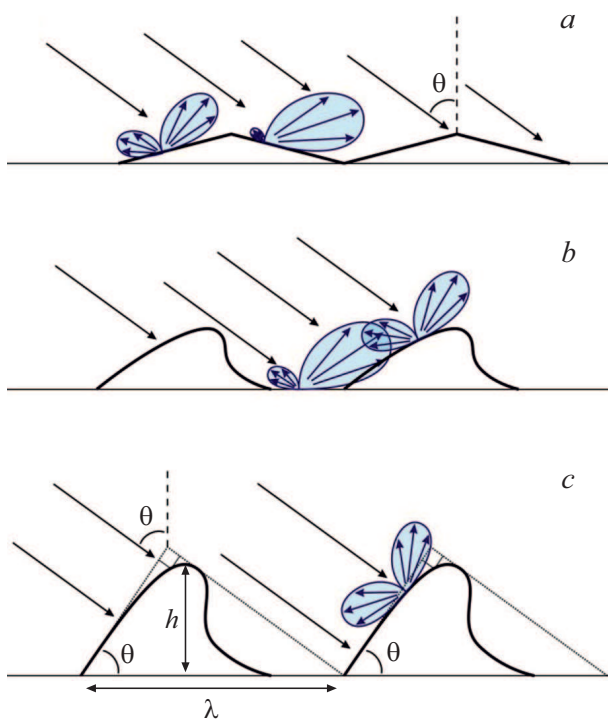


**Figure 6.** Schematic image of sputtering and reprecipitation at small fluences ($a$), intermediate fluences ($b$) and when shading by the wave crest with large fluences ($c$). The arrows show the directions of the clusters and the sputtering matter falling.

ripples obtained not with the same fluences, but with the same amount of sputtered matter. This would make it possible to compare the contributions of sputtering and redeposition to the process of relief formation. Therefore, let us consider further the sputtering yields of lithium niobate by gas cluster ions.

## 4.2. Sputtering yields

One of the tasks of the work was to study the sputtering yields $Y$ of lithium niobate by cluster ions and their relationship with the surface roughness. Data on $Y$ allows us to better understand the mechanisms of cluster ion sputtering and ripple formation; in addition, they are valuable in themselves for optimizing the processes of etching, smoothing and cleaning the surface.

The sputtering yield of cluster ions changes greatly with increasing size. The average cluster size in our experiments was 2500 atoms, but even for the same average sizes, $Y$ can vary due to different cluster size distributions. The exact distribution of clusters in the beam created by the ULVAC-PHI source is unknown. Therefore, in order to make our data on sputtering yields more relevant, the sputtering yield of the material with a known dependence $Y(E/n)$ was also measured and the results were compared with the literature.

For this purpose, measurements of $Y$ were made for SiO$_2$ films with a thickness of 100 nm, thermally grown on silicon. The amount of material removed is determined by the measurement methodology used. If $Y$ does not change with fluence $F_{ion}$, the thickness of the removed layer $z$ is related to the sputtering yield by a simple ratio

$$z = \frac{F_{ion}}{n_{at}} Y = \frac{It/eS}{n_{at}} Y, \qquad (8)$$

where $I$ — measured ionic current, $t$ — sputtering time, $S$ — the crater area (according to its dimensions at half-height, determined by the profilometer). In the case of a nonlinear dependence $z(F_{ion})$, $Y(F_{ion})$ can be calculated as the local slope of this dependence (the average of one-sided derivatives was used in the calculation). In the calculations, it was assumed that each cluster carries one

elementary charge, the atomic density of $n_{at}$ was taken to be $6.6 \cdot 10^{22}\,\text{cm}^{-3}$ for SiO$_2$ and $9.46 \cdot 10^{22}\,\text{cm}^{-3}$ for LiNbO$_3$.

The fluence required to remove the SiO$_2$ film with a thickness of 100 nm (i.e. at a fixed $z = 100$ nm) was estimated by XPS measurements carried out in parallel with the sputtering. It was assumed that it corresponds to a decrease in the intensity of the line O 1s by a factor of two. The calculated sputtering yields were 4.3 and 7.2 for 20 keV Ar$_{2500}^+$ with normal incidence ($\theta = 0°$) and oblique incidence ($\theta = 55°$), respectively. Yamada et al. reported a value of $Y = 3$ for 20 keV Ar$_{3000}^+$ with normal incidence and change of $Y$ with an increase in fluence (i.e. with the development of roughness) from 23 to 13 at $\theta = 60°$ [33]. The empirical formula proposed by Seah [37] gives $Y = 17.5$ for 8 eV/atom at $\theta = 45°$ (fluence unknown). Data on sputtering yields are also analyzed in [48]. Thus, our measurements of the sputtering yields SiO$_2$ correspond quite well to the data of the literature. In addition, it should be emphasized that ripples were observed at the bottom of the crater obtained at $\theta = 55°$, which reduces the accuracy of the determination of $Y$ by a method based on measurements of the film removal time by the XRS signal. A stylus profilometer was used to determine $Y$ of lithium niobate plates and the size of ripples according to AFM data was taken into account, which increases the accuracy of the experiment.

Measurements of lithium niobate sputtering yields at normal incidence yielded values of 0.71 for energy of 10 keV and 22 for 20 keV. In both cases, the surface became smoother (Table 2). But although much more material was removed by clusters with an energy of 20 keV scratches remained noticeable on the surface. Irradiation with an energy of 10 keV made it possible to remove scratches.

The shapes of the craters etched on LiNbO$_3$ by clusters with an energy of 10 keV at normal and oblique incidence are shown in Fig. 7. It is surprising that with an oblique incidence, the depth of the crater is „negative" (which is also reflected in Table 2).

This result is easily interpreted as ridges of ripples that have grown beyond the crater. The lateral resolution of the profilometer is not enough to resolve individual ripples, and the profilometer shows a protrusion instead of a crater. This result demonstrates that the growth of ripples is not due to a difference in local sputtering yields (as in Bradley−Harper theory for atomic ions), but implies an intensive redistribution of matter and its accumulation in protrusions. The matter is deposited on the protrusions faster than it is sputtered from them. Another finding is that determining the sputtering yield using a profilometer can significantly skew the results. The same can be said about methods based on measuring the thickness of films (ellipsometry [48], determination of the fluence necessary for film removal using SIMS or XPS [49]). Methods based on direct measurement of the sputtering mass (quartz microbalance [36]) are more reliable in this regard.

Next, the evolution of the sputtering yield with an increase in fluence in the case of an oblique incidence of
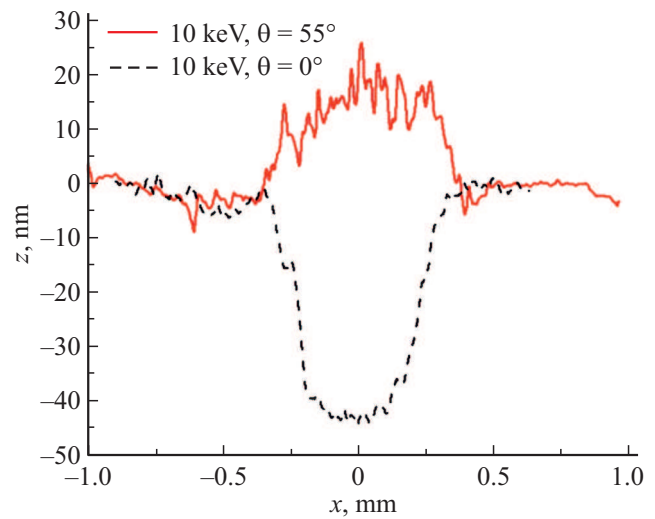


**Figure 7.** Forms of etching craters according to the profilometer.
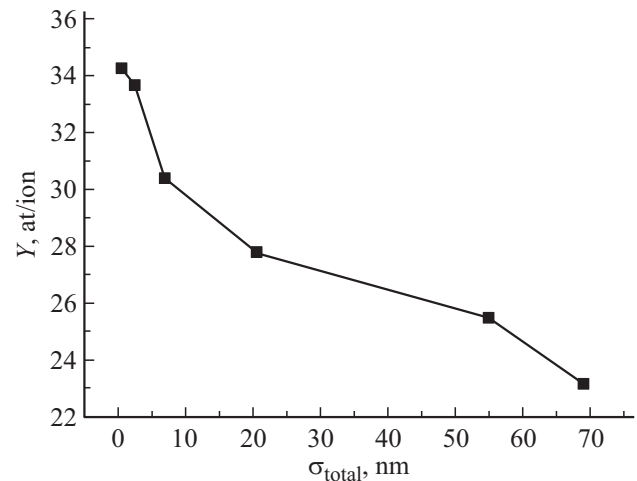


**Figure 8.** The dependence of the sputtering yields of clusters Ar$_{2500}^+$ 20 keV at $\theta = 55°$ on the roughness of the surface.

clusters with an energy of 20 keV was investigated. For a more accurate calculation of the $Y$, the topography of the crater bottom was taken into account according to AFM data. With low fluence, $Y(55°) = 34$, which is 1.5 times higher than $Y(0°)$. With an increase in fluence, the value of $Y$ decreased to 23, that is, almost to the value in a normal incidence, although, of course, it cannot be argued that reaching the value of $Y(0°)$ is a general rule. The reason for the change in the sputtering yield is the development of surface roughness. The correlation between the root mean square roughness and $Y$ is shown in Fig. 8.

Theoretically considering the influence of surface topography on the sputtering yield of atomic ions, Makeev and Barabasi [50] on the basis of Sigmund's theory integrated the energy deposit of the ion into the curved surface (similar to how the formation of the relief is considered as part of Bradley−Harper theory). They found that the curvature of

the surface can both decrease and increase $Y$. In the case of cluster ions, several mechanisms can be considered that affect the sputtering yield of a rough surface.

1) The dependence $Y$ on the local angle of incidence.

It was believed that the $Y$ monotonously falls with increasing angle [38]. However, at least for materials such as $SiO_2$, $KTiOPO_4$ [31] and $LiNbO_3$ it is now known that this dependence has a pronounced maximum at non-zero angles. Thus, at high fluences (Fig. 6, $c$), the cluster ion flying on the front side of the protrusion causes less sputtering. Assuming that for a flat surface $Y(55°)/Y(0°) = 1.5$, we get that this effect will reduce the sputtering yield of the surface with pronounced ripples by 1.5 times.

2) Blocking of sputtered atoms.

The distribution of the matter sputtered by the cluster ion is lateral, so the capture of this matter by protrusions on the surface is more significant than in the case of atomic ions. For the case shown in Fig. 6, $c$, up to half of the sputtered matter will be redeposited, further reducing the sputtering yield.

3) The influence of the curvature of the surface.

The length of the anterior slopes of ripples ($100-200$ nm) significantly exceeds the size of the area of interaction of the cluster with the matter ($\sim 10$ nm) [51]. However, some clusters collide with the tops of the protrusions, which will lead to an increase in the sputtering yield. The exact type of dependence of $Y$ on the curvature of the surface is unknown, so the contribution of this mechanism cannot be estimated.

Determination of sputtering yields makes it possible to compare the efficiency of ripple formation at different energy clusters. Considering that $Y(55°, 20\,keV)/Y(0°, 20\,keV) = Y(55°, 10\,keV)/Y(0°, 10\,keV)$ (of course, this is a rather rough estimate), we get that the amount of material removed at 10 keV, 55° corresponds to a depth of 40 nm (Table 2). The difference between this estimate and the measured depth ($-20$ nm) is consistent with the ripple height of 60 nm given in Table 1. The basic wavelengths are 546 nm and 873 nm (Table 1). Data for sputtering with an energy of 20 keV show that at this energy, $200-300$ nm of material must be removed to form ripples with the same wavelength. The same can be said for the values of $\sigma_{sh}$. Thus, although large fluences are required to form ripples at lower cluster energy, less material must be sputtered. The redistribution of mass becomes more significant compared to the actual sputtering. For the same reason, irradiation of the surface with clusters at $\theta = 0°$, 10 keV resulted in the removal of scratches as a result of mass redistribution. The effect of energy on the formation of ripples can be compared with the data [32], where the energy and size of the clusters changed simultaneously, and in the high specific energy mode the ripples were not detected.

## 4.3. Local piezoresponse of surface with ripples

Figure 9 shows the distributions of piezoresponses of the original surface and the surface with the most pronounced
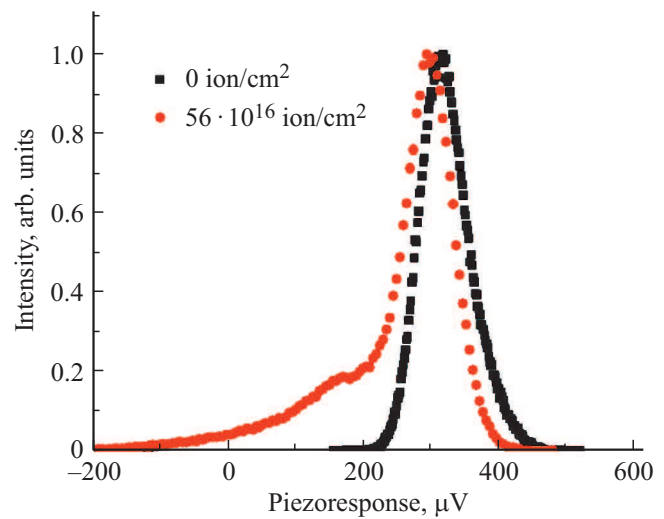


**Figure 9.** Distributions of the piezoresponse signal of the original surface and the surface with the most pronounced ripples.

ripples. The left arm of the curve corresponding to the irradiated surface arose due to the significant roughness of the surface. The probe reacted to sudden changes in altitude, which was mistakenly interpreted by the system as the result of deformation under the action of the applied voltage.

The maximum distribution practically did not change its position, therefore, the level of piezoresponse did not change much as a result of the formation of ripples with a height of 300 nm. We note that the resolution of the technique for depth on lithium niobate was investigated in [52], where it was shown that the damaged surface layer with a thickness of $0.4\,\mu m$ completely masks the piezoresponse signal, and a much thinner layer noticeably weakens it. Therefore, it can be concluded that the damaged layer of matter, which inevitably covers the irradiated surface, is quite thin. The surface of lithium niobate, covered with ripples, retains piezoelectric properties and can be used in nonlinear optics, devices based on surface acoustic waves, etc.

## 5. Conclusion

Ripples arising on the surface of lithium niobate during irradiation with cluster ions have been studied in detail. Their growth to a height of 350 nm and a wavelength of $1.4\,\mu m$ is shown. The wavelength-to-height ratio decreased, although a value consistent with the shading condition was not achieved. With an increase in fluence, the slope of the anterior slope of the protrusions approached perpendicular to the direction of ion incidence, and the rear slope was oriented along the beam. A bimodal distribution of ripples by wavelengths was found, especially noticeable in small fluences, and not previously observed on other materials.

The sputtering yield of lithium niobate by cluster ions at incidence angles of 0° and 55° from the normal to

the surface have been determined. The sputtering yield at oblique incidence $Y(55°)$ was 1.5 times higher than the $Y(0°)$, and as the ripples developed, it decreased to $Y(0°)$. The mechanisms responsible for such a change in the sputtering yield are proposed: this is the dependence of the $Y$ on the local angle of incidence, the blocking of emitted atoms and the influence of the curvature of the surface.

Ripples formed at the energy of clusters of 10 keV protruded from the crater of etching, which led to „negative" depth of the crater according to the stylus profilometer. This result highlights that surface elevation is particularly important to consider when determining the sputtering yields of cluster ions. In addition, it shows the importance of the contribution of the material redistribution process to the formation of ripples compared to the actual sputtering.

The results obtained speak in favor of the mechanism of ripple formation proposed by Postawa et al. [25] and based on mass redistribution dependent on local angles. However, note that in large fluences, nonlocal redistribution as a result of precipitation of the sputtered matter prevails over local. An important role is also played by sputtering: since $Y$ with a direct local angle of the incidence of the cluster is less, and in acute, at the beginning of the formation of ripples, their anterior slope is sputtered more slowly than the opposite.

According to piezoresponse microscopy, the surfaces of lithium niobate coated with ripples retained their piezoelectric properties virtually unchanged.

## Funding

## Conflict of interest

The authors declare that they have no conflict of interest.

# References

[1] I. Yamada. Mater. Sci. Eng. R **34**, 231 (2001). https://doi.org/10.1016/S0927-796X(01)00034-1

[2] A.E. Ieshkin, A.B. Tolstoguzov, N.G. Korobeishchikov, V.O. Pelenovich, V.S. Chernysh. Uspekhi Fiz. Nauk. (2022). https://doi.org/10.3367/UFNr.2021.06.038994

[3] I. Yamada, J. Matsuo, N. Toyoda, T. Aoki, E. Jones, Z. Insepov. Mater. Sci. Eng. A **253**, 249 (1998). https://doi.org/10.1016/s0921-5093(98)00733-3

[4] A.E. Ieshkin, A.A. Shemukhin, Yu.A. Ermakov, V.S. Chernysh. Vestn. MGU. Fizika, astronomiya **1**, 72 (2016) (in Russian). https://doi.org/10.3103/S0027134916010082

[5] V.S. Chernysh, A.E. Ieshkin, D.S. Kireev, A. V. Nazarov, A.D. Zavilgelsky. Surf. Coatings Technol. **388**, 125608 (2020). https://doi.org/10.1016/j.surfcoat.2020.125608

[6] A. Delcorte, V. Delmez, C. Dupont-Gillain, C. Lauzin, H. Jefford, M. Chundak, C. Poleunis, K. Moshkunov. Phys. Chem. Chem. Phys. **22**, 17427 (2020). https://doi.org/10.1039/d0cp02398a

[7] J.Y. Baek, C.M. Choi, S.J. Lee, B.K. Min, H.S. Kang, D.C. Choo, J.Y. Sung, J.S. Jin, M.C. Choi. Appl. Surf. Sci. **507**, 144887 (2020). https://doi.org/10.1016/j.apsusc.2019.144887

[8] O. Romanyuk, I. Gordeev, A. Paszuk, O. Supplie, J.P. Stoeckmann, J. Houdkova, E. Ukraintsev, I. Bartoš, P. Jiříček, T. Hannappel. Appl. Surf. Sci. **514**, 145903 (2020). https://doi.org/10.1016/j.apsusc.2020.145903

[9] D.F. Yancey, C. Reinhardt. J. Electron Spectros. Rel. Phenomena **231**, 104 (2019). https://doi.org/10.1016/j.elspec.2018.01.005

[10] A.E. Ieshkin, D.S. Kireev, A.A. Tatarintsev, V.S. Chernysh, B.R. Senatulin, E.A. Skryleva. Surf. Sci. **700**, 121637 (2020). https://doi.org/10.1016/j.susc.2020.121637

[11] E.A. Skryleva, B.R. Senatulin, D.A. Kiselev, T.S. Ilina, D.A. Podgorny, Y.N. Parkhomenko. Surf. Interfaces **26**, 101428 (2021). https://doi.org/10.1016/j.surfin.2021.101428

[12] V.Ya. Shur, E.V. Nikolaeva, E.I. Shishkin, V.L. Kozhevnikov, A.P. Chernykh. FTT **44**, *11*, 2055 (2002) (in Russian).

[13] K.E. Ozerova, A.A. Tatarintsev, E.I. Rau, K.F. Minnebayev, S.V. Zaitsev. Izv. RAN. Ser. fiz. **85**, *8*, 1074 (2021) (in Russian).

[14] G. Namkoong, K.K. Lee, S.M. Madison, W. Henderson, S.E. Ralph, W.A. Doolittle. Appl. Phys. Lett. **87**, 1 (2005). https://doi.org/10.1063/1.2084340

[15] A. Kakekhani, S. Ismail-Beigi, E.I. Altman. Surf. Sci. **650**, 302 (2016). https://doi.org/10.1016/j.susc.2015.10.055

[16] S. Sanna, W.G. Schmidt. J. Phys. Condens. Matter. **29**, 413001 (2017). https://doi.org/10.1088/1361-648X/aa818d

[17] N. Toyoda, B. Tilakaratne, I. Saleem, W.K. Chu. Appl. Phys. Rev. **6**, 020901 (2019). https://doi.org/10.1063/1.5030500

[18] R. Cuerno, J.S. Kim. J. Appl. Phys. **128**, 180902 (2020). https://doi.org/10.1063/5.0021308

[19] Q. Huang, Q. jia, J. Feng, H. Huang, X. Yang, J. Grenzer, K. Huang, S. Zhang, J. Lin, H. Zhou, T. You, W. Yu, S. Facsko, P. Jonnard, M. Wu, A. Giglia, Z. Zhang, Z. Liu, Z. Wang, X. Wang, X. Ou. Nature Commun. **10**, 2437 (2019). https://doi.org/10.1038/s41467-019-10095-2

[20] R.M. Bradley, J.M.E. Harper. J. Vac. Sci. Technol. A **6**, 2390 (1988). https://doi.org/10.1116/1.575561

[21] J. Muñoz-García, L. Vázquez, M. Castro, R. Gago, A. Redondo-Cubero, A. Moreno-Barrado, R. Cuerno. Mater. Sci. Eng. R **86**, 1 (2014). https://doi.org/10.1016/j.mser.2014.09.001

[22] S.Y. Siew, E.J.H. Cheung, H. Liang, A. Bettiol, N. Toyoda, B. Alshehri, E. Dogheche, A.J. Danner. Opt. Express **26**, 4421 (2018). https://doi.org/10.1364/oe.26.004421

[23] M. Qu, Y. Shen, L. Wu, X. Fu, X. Cheng, Y. Wang. Precis. Eng. **62**, 10 (2020). https://doi.org/10.1016/j.precisioneng.2019.11.001

[24] A. Osipov, S. Alexandrov, V. Berezenko, A. Speshilova, V. Alexandr, A. Osipov. Sensors Actuators A **337**, 113146 (2021). https://doi.org/10.1016/J.SNA.2021.113146

[25] D. Maciazek, M. Kanski, Z. Postawa. Anal. Chem. **10**, 4379 (2020). https://doi.org/10.1021/acs.analchem.0c01219

[26] N. Toyoda, I. Yamada. Mater. Res. Soc. Symp. Proc. **849**, 109 (2005). https://doi.org/10.1557/proc-849-kk7.9

[27] B.P. Tilakaratne, Q.Y. Chen, W.K. Chu. Materials **10**, 1056 (2017). https://doi.org/10.3390/ma10091056

[28] O. Lozano, Q.Y. Chen, B.P. Tilakaratne, H.W. Seo, X.M. Wang, P.V. Wadekar, P. V. Chinta, L.W. Tu, N.J. Ho, D. Wijesundera, W.K. Chu. AIP Adv. **3**, 062107 (2013). https://doi.org/10.1063/1.4811171

[29] D.S. Kireev, A.E. Ieshkin, A.A. Shemukhin. Pis'ma v ZhTF **46**, *9*, 3 (2020) (in Russian). https://doi.org/10.21883/PJTF.2020.09.49362.18021

[30] A. Ieshkin, D. Kireev, K. Ozerova, B. Senatulin. Mater. Lett. **272**, 127829 (2020). https://doi.org/10.1016/j.matlet.2020.127829

[31] I. V. Nikolaev, N.G. Korobeishchikov, M.A. Roenko. J. Phys. Conf. Ser. **1382**, 3 (2019). https://doi.org/10.1088/1742-6596/1382/1/012162

[32] I.V. Nikolaev, N.G. Korobeishchikov. Appl. Nano **2**, 25 (2021). https://doi.org/10.3390/applnano2010003

[33] K. Sumie, N. Toyoda, I. Yamada. Nucl. Instrum. Meth. B **307**, 290 (2013). https://doi.org/10.1016/j.nimb.2013.01.087

[34] H.M. Urbassek, R.M. Bradley, M.L. Nietiadi, W. Möller. Phys. Rev. B **91**, 165418 (2015). https://doi.org/10.1103/PhysRevB.91.165418

[35] V.I. Shulga. Appl. Surf. Sci. **458**, 18 (2018). https://doi.org/10.1016/j.apsusc.2018.07.059

[36] P.J. Cumpson, J.F. Portoles, A.J. Barlow, N. Sano. J. Appl. Phys. **114**, 124313 (2013). https://doi.org/10.1063/1.4823815

[37] M.P. Seah. J. Phys. Chem. C **117**, 12622 (2013). https://doi.org/10.1021/jp402684c

[38] H. Kitani, N. Toyoda, J. Matsuo, I. Yamada. Nucl. Instrum. Meth. B **121**, 489 (1997). https://doi.org/10.1016/S0168-583X(96)00556-3

[39] L. Rzeznik, R. Paruch, B.J. Garrison, Z. Postawa. Nucl. Instrum. Meth. B **269**, 1586 (2011). https://doi.org/10.1016/j.nimb.2010.11.098

[40] N.K. Sahoo, S. Thakur, R.B. Tokas. Thin Solid Films **503**, 85 (2006). https://doi.org/10.1016/j.tsf.2005.11.107

[41] A. Ieshkin, D. Kireev, V. Chernysh, A. Molchanov, A. Serebryakov, M. Chirkin. Surf. Topogr. Metrol. Prop. **7**, 025016 (2019). https://doi.org/10.1088/2051-672X/ab1f49

[42] D. Nečas, P. Klapetek. Cent. Eur. J. Phys. **10**, 181 (2012). https://doi.org/10.2478/s11534-011-0096-2

[43] A. Duparré, E. Quesnel, J. Ferré-Borrull. Appl. Opt. **40**, *13*, 2190 (2001). https://doi.org/10.1364/AO.40.002190

[44] E.L. Church, P.Z. Takacs. Proc. SPIE **1530**, 71 (1991). https://doi.org/10.1117/12.50498

[45] G. Rasigni, F. Varnier, M. Rasigni, J.P. Palmari, A. Llebaria. Phys. Rev. B **27**, 819 (1983). https://doi.org/10.1103/PhysRevB.27.819

[46] X. Zeng, V. Pelenovich, B. Xing, R. Rakhimov, W. Zuo, A. Tolstogouzov, C. Liu, D. Fu, X. Xiao. Beilstein J. Nanotechnol. **11**, 383 (2020). https://doi.org/10.3762/bjnano.11.29

[47] N. Toyoda, H. Kitani, N. Hagiwara, T. Aoki, J. Matsuo, I. Yamada. Mater. Chem. Phys. **54**, 262 (1998). https://doi.org/10.1016/S0254-0584(98)00101-1

[48] N.G. Korobeishchikov, I.V. Nikolaev, M.A. Roenko, V.V. Atuchin. Appl. Phys. A **124**, 833 (2018). https://doi.org/10.1007/s00339-018-2256-3

[49] L. Yang, M.P. Seah, I.S. Gilmore. J. Phys. Chem. C **116**, 23735 (2012). https://doi.org/10.1021/jp307203f

[50] M.A. Makeev, A.L. Barabási. Nucl. Instrum. Meth. B **222**, 335 (2004). https://doi.org/10.1016/j.nimb.2004.02.028

[51] V.N. Popok, I. Barke, E.E.B.B. Campbell, K.H. Meiwes-Broer. Surf. Sci. Rep. **66**, 347 (2011). https://doi.org/10.1016/j.surfrep.2011.05.002

[52] F. Johann, Y.J. Ying, T. Jungk, Á. Hoffmann, C.L. Sones, R.W. Eason, S. Mailis, E. Soergel. Appl. Phys. Lett. **94**, 3 (2009). https://doi.org/10.1063/1.3126490